Earth, Planets and Space

EXPRESS LETTER

Open Access

Coastal tsunami prediction in Tohoku region, Japan, based on S-net observations using artificial neural network

Yuchen Wang[1,2*], Kentaro Imai[1], Takuya Miyashita[3], Keisuke Ariyoshi[1], Narumi Takahashi[1,4] and Kenji Satake[2]

Abstract

We present a novel method for coastal tsunami prediction utilizing a denoising autoencoder (DAE) model, one of the deep learning algorithms. Our study focuses on the Tohoku coast, Japan, where dense offshore bottom pressure gauges (OBPGs), called S-net, are installed. To train the model, we generated 800 hypothetical tsunami scenarios by employing stochastic earthquake models (M7.0–8.8). We used synthetic tsunami waveforms at 44 OBPGs as input and the waveforms at four coastal tide gauges as output. Subsequently, we evaluated the model's performance using 200 additional hypothetical and two real tsunami events: the 2016 Fukushima earthquake and 2022 Tonga volcanic tsunamis. Our DAE model demonstrated high accuracy in predicting coastal tsunami waveforms for hypothetical events, achieving an impressive quality index of approximately 90%. Furthermore, it accurately forecasted the maximum amplitude of the 2016 Fukushima tsunami, achieving a quality index of 91.4% at 15 min after the earthquake. However, the prediction of coastal waveforms for the 2022 Tonga volcanic tsunami was not satisfactory. We also assessed the impact of the forecast time window and found that it had limited effects on forecast accuracy. This suggests that our method is suitable for providing rapid forecasts soon after an earthquake occurs. Our research is the first application of an artificial neural network to tsunami prediction using real observations. In the future, we will use more tsunami scenarios for model training to enhance its robustness for different types of tsunamis.

Keywords Tsunami early warning, Denoising autoencoder model, Offshore bottom pressure gauge, 2016 Fukushima tsunami, 2022 Tonga volcanic tsunami

*Correspondence:
Yuchen Wang
ywang@jamstec.go.jp
Full list of author information is available at the end of the article

Graphical Abstract

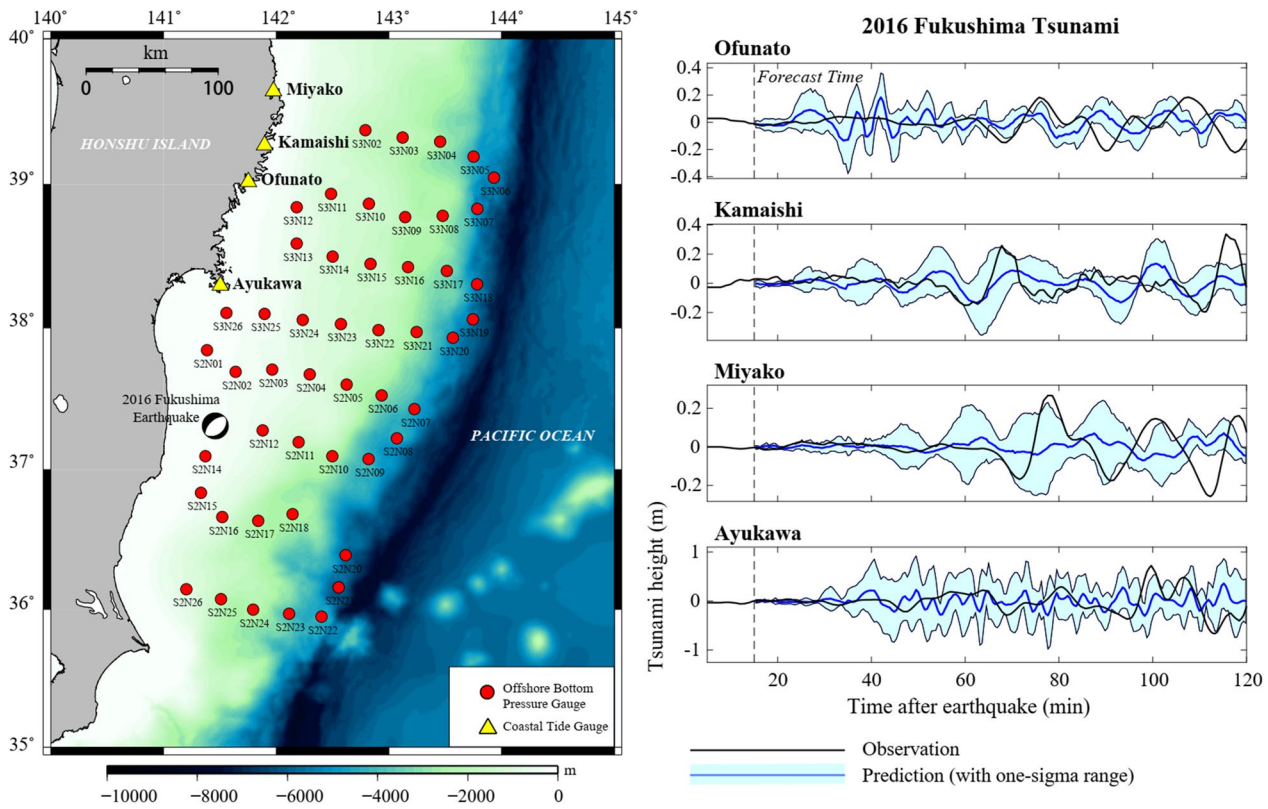

Introduction

In the wake of the catastrophic 2004 Indian Ocean and 2011 Tohoku tsunamis, offshore observational systems have been extensively installed to monitor earthquakes and tsunamis. These systems play a crucial role in providing direct information about tsunamis before they reach the coasts, enabling reliable and timely tsunami forecasting. For example, the Seafloor Observation Network for Earthquakes and Tsunamis along the Japan Trench (S-net) was launched in 2011 and completed in 2017 (Aoi et al. 2019; Kanazawa 2013). Comprising 150 cable-linked seismic and tsunami observatories, it is the world's largest offshore observation network for earthquakes and tsunamis and covers a vast area of approximately 1000 km × 300 km along the Pacific offshore of eastern Japan. S-net is divided into six subsystems, labeled S1 to S6, which are located off Chiba, off Ibaraki and Fukushima, off Miyagi and Iwate, off northern Sanriku, off Hokkaido and Aomori, and outer rise along the Japan Trench, respectively (Aoi et al. 2019). The S-net offshore bottom pressure gauges (OBPGs) are highly sensitive that can detect tsunamis with amplitudes of less than 1 cm. They recorded the tsunamis of the 2016 Fukushima earthquake (Mw 7.4; Wang and Satake 2021), the 2016 offshore Sanriku earthquake (Mw 6.0; Kubota et al. 2020), and the 2022 Tonga volcanic eruption (Tanioka et al. 2022; Wang et al. 2023).

Several tsunami forecasting algorithms have been developed based on offshore tsunami observational systems. Tsushima et al. (2009) proposed a near-field tsunami forecasting method using tsunami waveform inversion, called tsunami Forecasting based on Inversion for initial sea-Surface Height (tFISH). This method inverts observed tsunami waveforms at OBPGs for the initial sea-surface height distribution and then forecasts the coastal tsunami waveforms through a linear superposition of pre-computed Green's functions. Maeda et al. (2015) used an optimal interpolation algorithm for tsunami early warning, which assimilates offshore waveforms to reconstruct the tsunami wavefield and forecast coastal tsunami heights. This method does not require information about the initial tsunami source, but it is susceptible to coseismic deformation beneath the OBPGs (Maeda 2016). In a word, these forecasting algorithms

that utilize offshore tsunami data serve as valuable complements to the traditional early warning methods that rely on seismic wave observations.

Recently, deep learning algorithms have been applied to improve tsunami early warning systems. Mulia et al. (2020) employed a deep neural network architecture to analyze a tsunami inundation database of megathrust earthquakes along the Japan Trench. Their results achieved comparable accuracy to conventional physics-based simulations while reducing computational efforts by approximately 90%. Fauzi and Mizutani (2020) proposed a novel method for forecasting spatiotemporal tsunami wavefields by utilizing a deep predictive coding network and data assimilation. They demonstrated the effectiveness of this approach in predicting the 2011 Tohoku tsunami using synthetic waveforms at S-net stations. Liu et al. (2021) explored different machine learning approaches to forecast tsunami amplitudes at the Strait of Juan de Fuca, Canada, achieving very good predictions in a short time. Furthermore, Mulia et al. (2022) developed a connected neural networks-based method that utilizes S-net offshore observations to predict tsunami inundation at seven coastal cities in Japan, achieving comparable accuracy to physics-based models with a 99% reduction in computational costs. Although these studies used synthetic waveforms, they demonstrated the potential of deep learning algorithms in improving the efficiency and accuracy of tsunami early warning systems.

In this study, we employed a deep learning algorithm based on the denoising autoencoder (DAE) model for the purpose of coastal tsunami prediction in the Tohoku region, Japan. Synthetic tsunami waveforms from hypothetical events were employed to train the DAE model, while both synthetic waveforms and real observations (2016 Fukushima earthquake and 2022 Tonga volcanic tsunamis) were used for model testing. Notably, this research is the first to apply a deep learning algorithm to tsunami prediction using real offshore observations. Deep learning technique achieves accurate coastal tsunami prediction without relying on prior information regarding the tsunami source or coseismic deformation.

Data

In this study, we used both synthetic and real data of S-net OBPGs. Synthetic data comprised tsunami waveforms simulated from 1,000 stochastic earthquake models (M7.0–8.8) offshore the Tohoku region, Japan. We randomly divided the data into two subsets: 80% for training our model and 20% for testing. On the other hand, real data used in this study were obtained from observations of two tsunamis, namely, the 2016 Fukushima earthquake and 2022 Tonga volcanic tsunamis. The 2016 Fukushima earthquake took place on November 22, 2016, offshore the Tohoku region (Fig. 1). The earthquake was characterized as a normal faulting event (Adriano et al 2018). It led to a moderate tsunami, which was subsequently detected by both tide gauges and OBPGs in Japan. This is the largest tsunami event since the installation of S-net. Fortunately, no casualties were reported because of its moderate magnitude. The 2022 Tonga volcanic tsunami was caused by the submarine eruption of the Hunga Tonga–Hunga Ha'apai volcano on January 15, 2022. This event had a complex generating mechanism, posing difficulties in traditional tsunami early warning algorithms based on source inversion.

Real data

We selected 44 S-net stations from S2 and S3 groups (Fig. 1) as the input. These stations recorded sea level changes during the 2016 and 2022 tsunami events (Additional file 1: Figures S1 and S2). The S-net data have a high sampling rate of 0.1 s, which we resampled to 10-s intervals to reduce computational costs. To emulate the real-time operation as closely as possible, we refrained from using a band-pass filter to process the raw data. Instead, we performed only polynomial interpolation to eliminate the tidal signal, following the methodology outlined by Mofjeld (1997). This operation can be easily executed in real time. Additionally, the seismic waves can interfere with the OBPG records, making it difficult to distinguish tsunami signals, especially at stations near the earthquake source area (Wang et al. 2020). Thus, we omitted the first 5 min of pressure waveforms for the 2016 Fukushima tsunami data, during which the seismic wave disturbance predominantly occurred (Mulia et al. 2022). Regarding the 2022 Tonga volcanic tsunami, which is a non-seismogenic event, the selection of time series was not based on the occurrence time of the earthquake. Instead, we selected OBPG records specifically from the period commencing at 13:00 (UTC) on January 15, 2022, corresponding to the time when the evident tsunami peak reached S-net stations, as noted by Wang et al. (2023).

Besides S-net stations, we selected four coastal stations in the Tohoku region, Kamaishi, Ofunato, Miyako, and Ayukawa (Fig. 1), to validate our approach through waveform comparison. We used real data from the 2016 Fukushima earthquake and 2022 Tonga volcanic tsunamis. Tide gauge records for Kamaishi were acquired from the Japan Oceanographic Data Center with a sampling rate of 30 s, while records for Ofunato were obtained from the Intergovernmental Oceanographic Commission with a sampling rate of 60 s. The Japan Meteorological Agency provided us with records for Miyako and Ayukawa, also with a sampling rate of 60 s. The data were processed

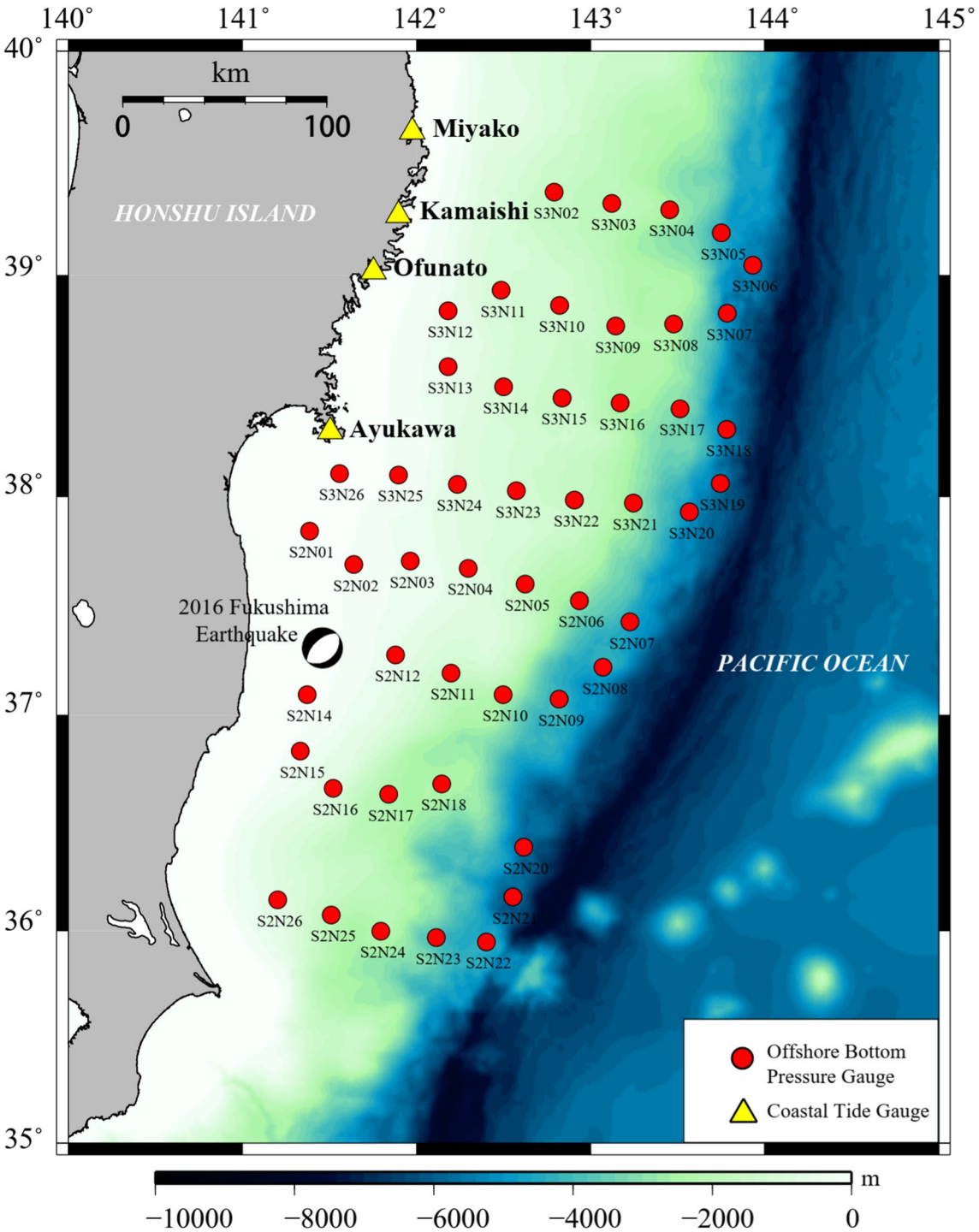

Fig. 1 Map of the study area, featuring offshore bottom pressure gauges (represented by red circles) and coastal tide gauges (represented by yellow triangles). The tsunami waveforms at offshore bottom pressure gauges are used as input data, and the waveforms at coastal tide gauges are output data. The focal mechanism for the 2016 Fukushima earthquake was derived from the Global Centroid Moment Tensor catalog. (https://www.globalcmt.org/)

through polynomial fitting to eliminate tidal components in a similar manner to S-net data.

Synthetic data

We adopted a stochastic earthquake source model to compute synthetic tsunamis. The stochastic model facilitates the creation of possible source models, correlating with the slip distributions of historical subduction earthquakes based on by Goda et al. (2014). It is investigated that the spectral characteristics of slip distributions of historical earthquakes, inferred by inversion analyses, can be approximated using von Karman-type spectra and several parameters. When this standard spectral shape is employed with random phases, a two-dimensional slip distribution is randomly generated and positioned randomly within the boundaries of a presumed fault plane. If the distribution satisfies specific constraints related to the properties of historical earthquakes, it is considered as one potential source within the region. Repeating this generation method can develop an arbitrary number of source models (Goda et al. 2016).

We employed 1000 stochastic models, located along the Japan Trench. The fault model covered a 650 km × 250 km area consisting of 65 × 25 subfaults. Each subfault had a constant strike of 193° and constant rake of 90°. Dip angles varied from 8° to 16°, gradually steepening along the down-dip direction. With varying dip angles, the subfaults closest to the trench axis had a depth of 0 km, while the deepest subfaults had a depth of 54 km (Mai and Thingbaijam 2014). The hypothetical sources did not cover the entire size of the fault area, but were randomly located within the area (see Additional file 1: Figure S3). Because thrust faulting (reverse faulting) is the dominant faulting mechanism at the interface between the subducting oceanic plate and the overriding continental plate, the stochastic model only considered thrust faulting earthquake (Goda et al. 2016). The magnitudes ranged from 7.0 to 8.8, with intervals of 0.2, and there were 100 scenarios for each magnitude. We plotted the locations of rectangular faults and the slip distribution of a hypothetical earthquake scenario in Additional file 1: Figure S3. The tsunami waveforms of 44 S-net stations and four coastal tide gauges were calculated in accordance with the locations of real observations. We subtracted the initial displacement at each station location from the resulting tsunami waveforms to mimic pressure waveforms. This process introduced a constant offset in the pressure readings, which reflects the coseismic deformation that occurred at stations inside the source region. This effect is one of the primary challenges in using tsunami data assimilation for early warning systems (Maeda 2016). Although synthetic tsunami waveforms are free from seismic wave disturbances, we still excluded the first 5 min after the earthquake for model training and testing.

Method

Tsunami simulation

For each stochastic model, we used Okada's equations (Okada 1992) to calculate the deformation of the seafloor, with an assumption that the displacement of the sea surface was the same as that of the seafloor. We then implemented the linear long-wave equations to simulate the propagation of the tsunami, which was achieved by the *JAGURS* code (Baba et al. 2015).

We implemented a four-layer nested bathymetric grid system, beginning with a region-wide first layer featuring a grid size of 18 arc sec (~ 555 m), derived from the General Bathymetric Chart of the Ocean. The S-net OBPG waveforms were computed within this layer. The subsequent three layers were composed of finer grids with a grid size of 6 arc sec (~ 185 m), 2 arc sec (~ 60 m), and 0.667 arc sec (~ 20 m), respectively, which covered the coastal tide gauges. The grids of these three layers were derived from the M7000 Digital Bathymetric Chart from the Japan Hydrographic Association. During numerical simulation, we adopted a time step of 0.25 s. Following this, we resampled the synthetic waveforms of the S-net OBPGs to a 10-s interval, while the synthetic waveforms of the coastal tide gauges were resampled to a 1-min interval.

Model training

DAE model comprises an encoder and a decoder, which work together to denoise or correct corrupted input data (Goodfellow et al. 2016). The encoder maps the input data into a lower-dimensional representation, while the decoder maps the lower-dimensional representation back into the original input space. The goal of the model is to learn a compressed representation of the input data that captures the most important features, while minimizing the reconstruction error between the original input and the output of the decoder. DAE models have been successfully used in various applications, including speech recognition, anomaly detection, and tsunami prediction (Liu et al. 2021).

The model takes as input tsunami waveforms recorded by OBPGs (i.e., S-net stations): $\boldsymbol{x} \in \mathbb{R}^{N_o \times L_{obs}}$. In this equation, N_o denotes the number of OBPGs used and L_{obs} represents the length of input data, which is defined as the *forecast time window* (FTW). We examined the performance of different FTWs ranging from 5 to 35 min. For seismogenic tsunamis, the first 5-min waveform after the earthquake was excluded from analysis. The model output, represented by the prediction for tsunami waveforms at coastal tide gauges, was denoted as

$\boldsymbol{y} \in \mathbb{R}^{N_{tg} \times L_{prd}}$. Here, N_{tg} and L_{prd} refer to the number of coastal stations and the length of output data, respectively. The waveforms were output up to 115 min after the beginning of the FTW (i.e., 120 min after the earthquake for seismogenic tsunamis).

We randomly selected 800 scenarios for model training out of 1000 hypothetical tsunamis. The training dataset can be represented as

$$\boldsymbol{X}_{train} = [\boldsymbol{x}_1, \boldsymbol{x}_2, \boldsymbol{x}_3, \ldots, \boldsymbol{x}_{800}], \boldsymbol{Y}_{train} = [\boldsymbol{y}_1, \boldsymbol{y}_2, \boldsymbol{y}_3, \ldots, \boldsymbol{y}_{800}]. \tag{1}$$

A data point ($\boldsymbol{x}_i$, $\boldsymbol{y}_i$) contains tsunami waveforms at OBPGs and coastal tide gauges. Our forecast models will take the following form:

$$f : \mathbb{R}^{N_o \times L_{obs}} \times \mathbb{R}^{N_{par}} \rightarrow \mathbb{R}^{N_{tg} \times L_{prd}}. \tag{2}$$

For each model parameter represented as $\boldsymbol{\theta} \in \mathbb{R}^{N_{par}}$, the function f maps the input to the output. The number of model parameters N_{par} is determined by the model itself, and the task of model training is to estimate the appropriate parameter $\boldsymbol{\theta}$ through a supervised learning procedure. The mean absolute error was used as the training loss without any regularization. The estimation is achieved via a stochastic gradient descent algorithm *Adam* developed by Kingma and Ba (2015). For more details about the structure of the DAE model, refer to Zhou and Paffenroth (2017).

When training deep neural networks, it is a common practice to partition the training set into minibatches (Goodfellow et al. 2016). A minibatch refers to a small subset of the training data (i.e., tsunami waveforms) that is used during each iteration of the training process to improve the computational and memory efficiency. We selected minibatches containing a maximum of 20 data points ($\boldsymbol{x}_i$, $\boldsymbol{y}_i$). In addition, we aimed to estimate the uncertainty in our forecasts. To achieve this, we trained an ensemble of autoencoders on the same training set, each with a randomly initialized set of weights. In deep learning, an epoch refers to an iteration through the entire training dataset during the training phase. During an epoch, the model processes each training example once and updates its parameters based on the computed gradients. The ensemble was trained for 400 epochs. The model training procedure was conducted using the *PyTorch* package and executed on the EIC supercomputer of Earthquake Research Institute.

Model testing

The remaining 200 hypothetical scenarios were used for model testing. The data format was consistent with the one of training dataset. Meanwhile, we included the real events of the 2016 Fukushima earthquake and 2022 Tonga volcanic tsunamis.

To forecast coastal tsunami waveforms, we employed an ensemble approach that utilizes the mean and variance of the output. Specifically, we used the sample mean of the autoencoder output as the prediction. The ensemble output, which reflects the uncertainty in parameter estimation, served as an indicator of the forecast uncertainty. The waveforms' one-sigma range was calculated.

The maximum amplitude is very important to tsunami early warning. We determined the maximum amplitude for each coastal tide gauge across 202 testing events using the output time series and compared the results against observations. In 200 hypothetical scenarios, we utilized the synthetic waveforms generated by forward simulation for comparison. We quantitatively evaluated the performance of our tsunami prediction using the quality index (QI) proposed by Tsushima et al. (2012):

$$QI = \left[1 - \frac{\sum_{i=1}^{N_{tg}} (O_i - P_i)^2}{\sum_{i=1}^{N_{tg}} (O_i)^2}\right] \times 100\%. \tag{3}$$

Here, O_i and P_i are the maximum amplitudes of the observed and predicted tsunami waveforms, respectively. A value of 100% indicates complete accuracy in prediction, but when predictions have significant deviations, it can result in negative values. We calculated QI for the 202 testing events. In addition, we compared the QI of tsunami prediction among different FTWs for 200 hypothetical scenarios and two real events.

Results

We first compared the observed and predicted waveforms of hypothetical events. The No. 461 event generated by an M7.8 earthquake was taken as an example (Fig. 2). The arrival time of the first peak at four coastal stations was approximately 30–40 min after the earthquake. During the later phase, some stations exhibited a slightly higher predicted amplitude than observations, but the difference was not deemed significant. Overall, the predicted waveforms closely matched the observed waveforms for both 10- and 25-min FTWs. Although there was a slight underestimation of the maximum amplitude at Ofunato, the observed waveform generally fell within the predicted waveform's one-sigma range. No noticeable differences were observed between the two FTWs. Both 10- and 25-min FTWs had a high QI of 97.6%.

Additionally, we compared the observed and predicted maximum amplitudes for all 200 hypothetical events as the scatter plots in Supplementary Material (Additional file 1: Figures S4 and S5). The predicted maximum amplitude was calculated by taking the average of the maximum values within each ensemble. We found

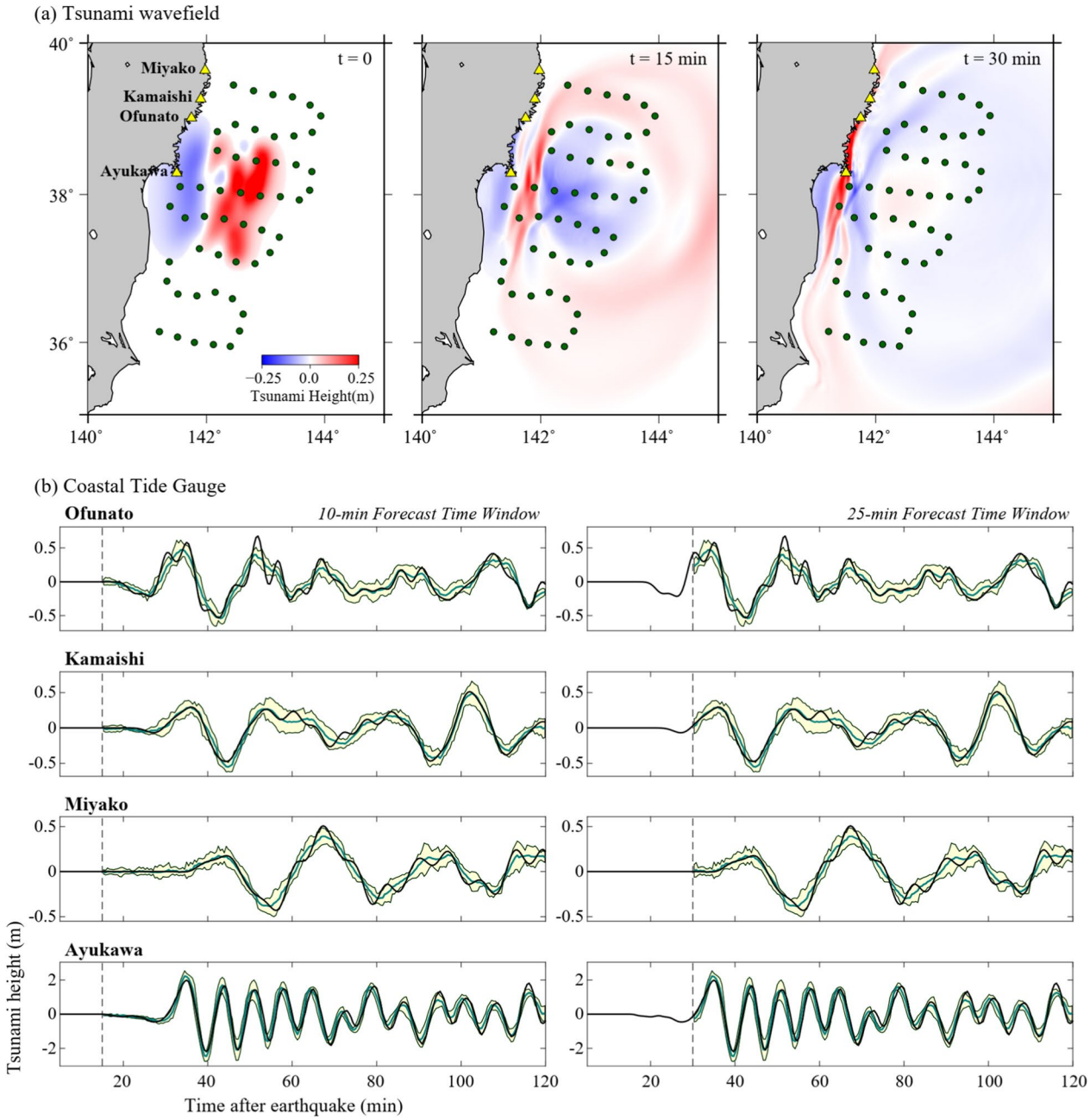

Fig. 2 **a** Wavefield of the No. 461 hypothetical tsunami at $t = 0$, 15, and 30 min. Yellow triangles represent coastal tide gauges. Dark green circles represent offshore bottom pressure gauges. **b** Observed (black) and predicted (green) waveforms of the No. 461 hypothetical tsunami at coastal tide gauges, considering forecast time windows of 10 min (left column) and 25 min (right column). As a hypothetical event, the observed waveforms were obtained by forward modeling. The range of one-sigma prediction is depicted by the light green color

no significant differences between the 10- and 25-min FTWs. Specifically, the discrepancies between the observed and predicted maximum amplitudes were smaller at Kamaishi and Miyako compared to Ofunato and Ayukawa. Considering the entire set of 200 hypothetical events, the QI was 90.9% (89.1–92.7%, 0.99 confidence interval) for a 10-min FTW and 90.8% (89.0–92.6%, 0.99 confidence interval) for a 25-min FTW.

Regarding the 2016 Fukushima tsunami, the observed waveforms also generally fell within the one-sigma range of the predicted waveform at four coastal stations (Fig. 3). At Ofunato, the predicted waveform aligned well with the

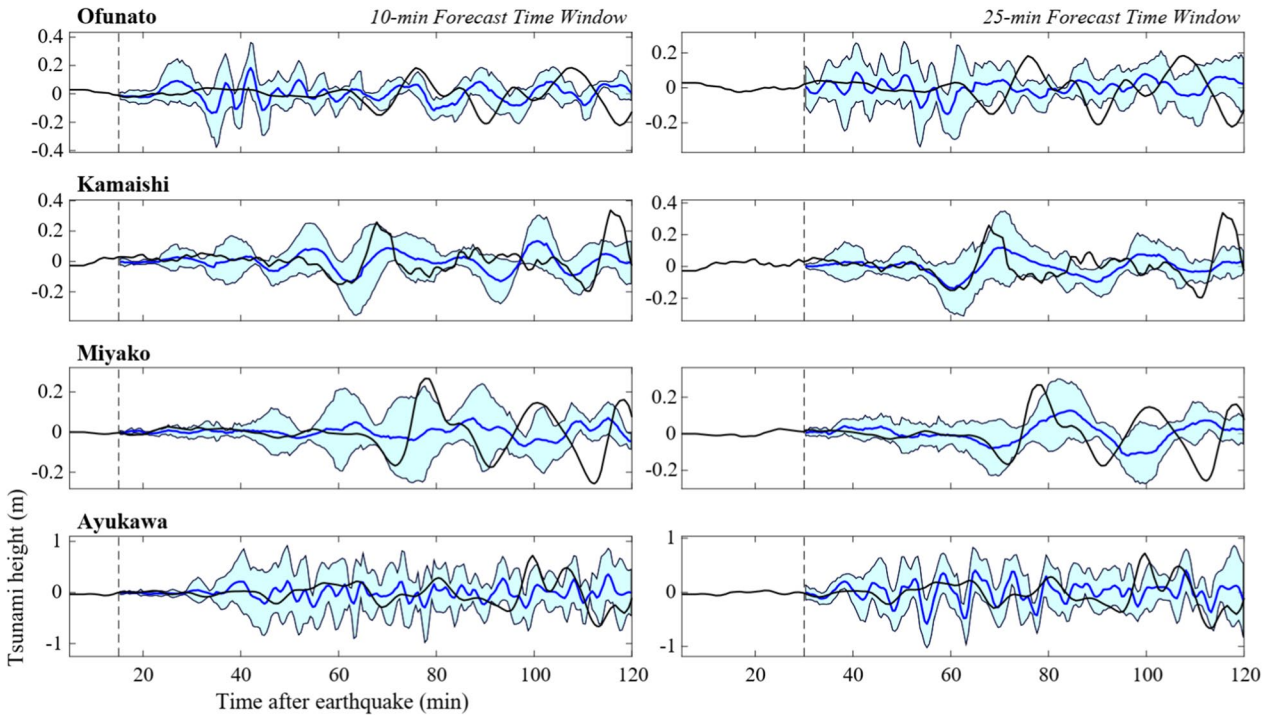

Fig. 3 Observed (black) and predicted (blue) waveforms of the 2016 Fukushima tsunami at coastal tide gauges, considering forecast time windows of 10 min (left column) and 25 min (right column). The range of one-sigma prediction is depicted by the light blue color

observations in a 10-min FTW, particularly in the following phases after 60 min. However, there was an underestimation of the amplitude in a 25-min FTW. At Kamaishi, both 10- and 25-min FTWs exhibited a slight underestimation of the tsunami amplitude. At Miyako, there was a significant underestimation of the amplitude in a 10-min FTW, but the predicted results improved in a 25-min FTW. At Ayukawa, the predicted waveform matched the observations quite well, although the predicted waveform contained more high-frequency components. The QI for the four stations was 91.4% and 92.4% for a 10- and 25-min FTW, respectively.

However, the results of the 2022 Tonga volcanic tsunami were unsatisfactory (Fig. 4). The tsunami was greatly overestimated at most coastal stations, and the predicted tsunami phases were not accurate (although this study primarily focuses on tsunami amplitude forecasting). Only at Ayukawa did the results show slight consistency. The QI was calculated as 50.2% for a 10-min FTW. In a 25-min FTW, the QI dropped to a negative value (− 25.6%), indicating an extremely poor forecasting performance.

Finally, we plotted the QI for various FTWs, ranging from 5 to 35 min (Fig. 5). The QI for the hypothetical events remains consistently high, averaging around 90% across different FTWs. Conversely, the QI for the 2016 Fukushima tsunami varies across different FTWs, yet it consistently exceeds 75% in all cases and does not surpass the upper limit of the confidence interval established by the hypothetical events. Due to its extremely poor performance, we refrained from plotting the QI for the 2022 Tonga volcanic tsunami, as it drops below zero in certain FTWs (detailed results are shown in Additional file 1: Table S1).

Discussion

The performance of the hypothetical events in the testing dataset demonstrated good accuracy in tsunami prediction. The DAE model accurately predicted the maximum height, and it showed a good match between the predicted waveforms and observations (i.e., forward simulation). Regarding the testing of real events, the model's prediction performance was satisfactory for the 2016 Fukushima tsunami, as the maximum height was mostly accurately predicted. Although there were some discrepancies between the predicted and observed waveforms, we mainly focus on the maximum amplitude, as it is the most important criterion in tsunami early warning. These findings provide evidence of the potential application of a tsunami early warning system using an artificial neural network based on offshore tsunami observations in the Tohoku region of Japan. The discrepancies between the prediction and observation of the 2016 Fukushima tsunami can be attributed to unexpected signals recorded by

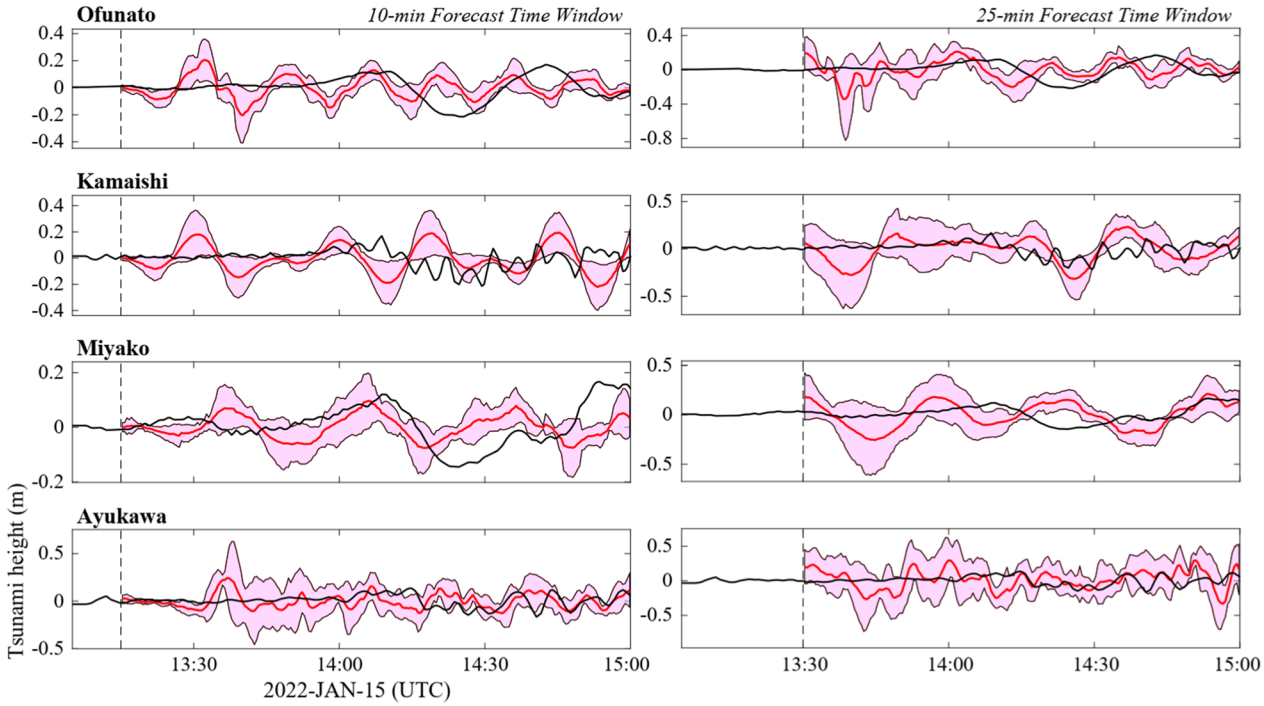

Fig. 4 Observed (black) and predicted (red) waveforms of the 2022 Tonga volcanic tsunami at coastal tide gauges, considering forecast time windows of 10 min (left column) and 25 min (right column). The range of one-sigma prediction is depicted by the light red color

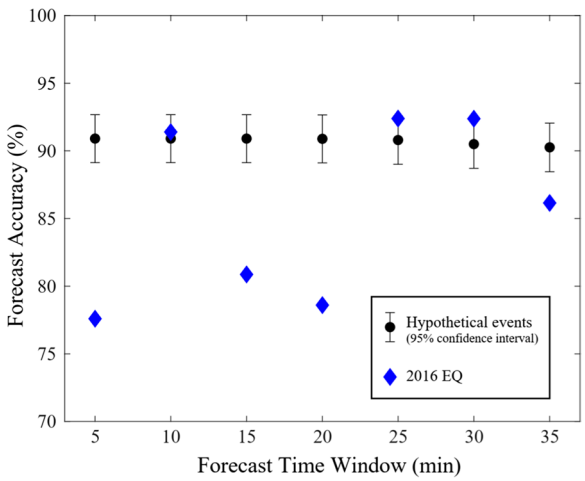

Fig. 5 Comparison of forecast accuracy (quality index) among different forecast time windows for 200 hypothetical tsunami events (black dots) and the tsunami of the 2016 Fukushima earthquake (blue diamonds)

OBPGs. Although the first 5 min after the earthquake has already been excluded, some unexpected signals that are not related to the tsunami arrival are still present in the input data. For example, S2N18 exhibits an anomalous decreasing trend in the first 20 min, and S2N11 displays an abrupt step in the waveform (Additional file 1: Figure S1). Kubota et al. (2020) suggested that these signals may result from mechanical issues of the observation system, as they are identical in the pair of pressure sensors (i.e., HP1WP, HP2WP) at each S-net station. The presence of such unexpected signals can introduce biases in the model testing results. Conversely, the tsunami scenarios generated with "clean" synthetic waveforms yield more accurate predictions compared to real events. Moreover, discrepancies may also arise from imperfect modeling due to the limitations of bathymetry data (Wang and Satake 2021). This is an unavoidable challenge that is not unique to the approach presented here, but also affects other methods of tsunami early warning, such as tFISH (Tsushima et al. 2009) and tsunami data assimilation (Maeda et al. 2015). Meanwhile, the 2016 Fukushima tsunami was generated by a normal faulting earthquake, which resulted in more subsidence in the initial sea-surface deformation (Kubota et al. 2021). This is different from the scenarios in the training dataset, which comprise thrust faulting earthquakes. This difference may limit the predictive capacity of the DAE model.

Nevertheless, the prediction of the 2022 Tonga volcanic tsunami was not successful, which can be attributed to its trans-oceanic natures. We conducted a synthetic experiment of the 2010 Maule earthquake (Mw 8.8), using the source model of Yoshimoto et al. (2016) (please see Additional file 1: Text S1 for more information). We recorded

the synthetic waveforms of S-net OBPGs as the input (Additional file 1: Figure S6) and predicted the coastal waveforms with 10- and 25-min FTWs (Additional file 1: Figure S7). Unfortunately, the results were as poorly as the Tonga event. The DAE model in this study was trained using a dataset consisting exclusively of near-field tsunamis resulting from earthquakes in the Japan Trench. However, trans-oceanic tsunamis are influenced by complicated effects such as dispersion, refraction, and diffraction during the propagation process, and the largest wave peaks often occur in the later phase (Additional file 1: Figure S6), which is different from the near-field tsunami that we use for training. This limited scope of training data may have hindered the model's performance in accurately predicting trans-Pacific tsunamis. Besides, the OBPG records of the 2022 Tonga volcanic tsunami were affected by atmospheric variations (Tanioka et al. 2022), leading to more potential bias in prediction. To improve the forecasting ability of the model for such events, additional scenarios of trans-oceanic tsunamis should be included in the training dataset. In fact, when considering trans-oceanic tsunamis reaching Japan (e.g., tsunamis triggered by large earthquakes in Chile), using tsunami observations near the source area as input rather than S-net OBPGs would yield more timely results become more efficient. The tsunami early warning could be issued much earlier before it arrives in Japan. Conversely, in the event of a large earthquake in Japan, we could conduct tsunami predictions for distant locations around the Pacific Ocean using the DAE model based on S-net observations.

Furthermore, FTW did not have evident effects on the forecast performance. Even a relatively short FTW can achieve prediction accuracy similar to that of a long FTW. Therefore, our approach is suitable for providing rapid forecast on coastal tsunami heights. During real-time application, the early warning system can be triggered by the seismic wave, enabling a prompt forecast to be generated shortly after an earthquake occurs. In contrast, successful tsunami prediction through data assimilation requires a significant amount of offshore data to reconstruct the tsunami wavefield. According to Wang and Satake (2021), a 35-min FTW is necessary to achieve satisfactory forecast results for the 2016 Fukushima earthquake, and the accuracy of the assimilation increases with longer FTW.

As a limitation of this study, we acknowledge that we did not incorporate some tide gauges near the epicenter (e.g., Onahama) because the tsunami arrived too early to test the 35-min FTW. Besides, we lack high-precision bathymetry data for these stations. Our study mainly focuses on stations along the Sanriku coast, located north of the seismic source. Therefore, our selection of stations was not comprehensive enough. However, our purpose of the paper is not to study this tsunami event, but rather test the method of early warning based on S-net data using artificial neural network. We also note that the DAE model is not limited to regions with a dense offshore observation system. Liu et al. (2021) showed that a single offshore station near the entrance of the Strait of Juan de Fuca, Canada, suffices the input data and then the waveform of stations inside the strait can be predicted. Moreover, to enhance the reliability of input data, we propose incorporating additional observational data besides OBPGs. For instance, real-time observations from the Global Navigation Satellite System could be considered, as suggested by Makinoshima et al. (2021) and Rim et al. (2022).

Conclusion

We successfully adopted a deep learning algorithm, the denoising autoencoder (DAE) model, to forecast tsunamis in the Tohoku region, Japan. Using offshore tsunami waveforms as input, we predicted coastal tsunamis at Kamaishi, Ofunato, Miyako, and Ayukawa, achieving an impressive accuracy rate of approximately 90% for synthetic tsunami waveforms generated by hypothetical earthquakes in the Japan Trench. The algorithm demonstrated a satisfactory accuracy of over 75% for the 2016 Fukushima tsunami 15 min after the earthquake (i.e., 10-min forecast time window). However, the performance of the 2022 Tonga volcanic tsunami was not satisfactory due to the limitation of its training set. This study marks the first application of a deep learning algorithm in tsunami prediction using real offshore observations. Our future endeavors will involve training the model with trans-oceanic tsunami scenarios and expanding its capabilities to encompass tsunamis of different sources.

Abbreviations

DAE	Denoising autoencoder
FTW	Forecast time window
OBPG	Offshore bottom pressure gauge
QI	Quality index
S-net	Seafloor Observation Network for Earthquakes and Tsunamis
tFISH	Tsunami Forecasting based on Inversion for initial sea-Surface Height

Supplementary Information

The online version contains supplementary material available at https://doi.org/10.1186/s40623-023-01912-6.

Additional file 1. Synthetic Experiment of the 2010 Maule Tsunami.

Acknowledgements

The authors thank Prof. Zhiyuan Ren and Prof. Hoiio Kong for their suggestions on deep learning model.

Author contributions

YW is responsible for formal analysis.

Funding
This work was supported by KAKENHI: Yuchen Wang 21K21353. This work was supported by the Core-to-Core Collaborative Research Program of the Earthquake Research Institute, the University of Tokyo, and the Disaster Prevention Research Institute, Kyoto University (2021-K-01 and 2023-K-02).

Availability of data and materials
The *JAGURS* code for computing synthetic tsunamis is available at https://github.com/jagurs-admin/jagurs. The S-net observations are available at https://doi.org/10.17598/NIED.0007. Hypothetical earthquake data are available at https://doi.org/10.6084/m9.figshare.23910249.

Declarations

Ethics approval and consent to participate
Not applicable.

Consent for publication
Not applicable.

Competing interests
The authors declare that they have no competing interests.

Author details
[1]Japan Agency for Marine–Earth Science and Technology, Yokohama, Kanagawa 236-0001, Japan. [2]Earthquake Research Institute, The University of Tokyo, Tokyo 113-0032, Japan. [3]Disaster Prevention Research Institute, Kyoto University, Uji, Kyoto 611-0011, Japan. [4]National Research Institute for Earth Science and Disaster Resilience, Tsukuba, Ibaraki 305-0006, Japan.

Received: 27 June 2023 Accepted: 26 September 2023
Published online: 08 October 2023

References

Adriano B, Fujii Y, Koshimura S (2018) Tsunami source and inundation features around Sendai Coast, Japan, due to the November 22, 2016 Mw 6.9 Fukushima earthquake. Geosci Lett 5:2. https://doi.org/10.1186/s40562-017-0100-9
Aoi S, Suzuki W, Chikasada NY, Miyoshi T, Arikawa T, Seki K (2019) Development and utilization of real-time tsunami inundation forecast system using S-net data. J Disaster Res 14:212–224. https://doi.org/10.20965/jdr.2019.p0212
Baba T, Takahashi N, Kaneda Y et al (2015) Parallel implementation of dispersive tsunami wave modeling with a nesting algorithm for the 2011 Tohoku tsunami. Pure Appl Geophys 172:3455–3472. https://doi.org/10.1007/s00024-015-1049-2
Fauzi A, Mizutani N (2020) Potential of deep predictive coding networks for spatiotemporal tsunami wavefield prediction. Geosci Lett 7:20. https://doi.org/10.1186/s40562-020-00156-7
Goda K, Mai PM, Yasuda T, Mori N (2014) Sensitivity of tsunami wave profiles and inundation simulations to earthquake slip and fault geometry for the 2011 Tohoku earthquake. Earth Planets Space 66:1–20. https://doi.org/10.1186/1880-5981-66-105
Goda K, Yasuda T, Mori N, Maruyama T (2016) New scaling relationships of earthquake source parameters for stochastic tsunami simulation. Coast Eng J 58:1650010-1-1650010–1650040. https://doi.org/10.1142/S0578563416500108
Goodfellow I, Bengio Y, Courville A (2016) Deep learning. MIT press. http://www.deeplearningbook.org. Accessed 2 May 2023.
Kanazawa T (2013) Japan Trench earthquake and tsunami monitoring network of cable-linked 150 ocean bottom observatories and its impact to earth disaster science. In: Proceedings of the 2013 IEEE international underwater technology symposium (UT), Tokyo, Japan. https://doi.org/10.1109/UT.2013.6519911.
Kingma DP, Ba J (2015) Adam: a method for stochastic optimization. https://arxiv.org/abs/1412.6980. Accessed 2 May 2023.
Kubota T, Kubo H, Yoshida K, Chikasada NY, Suzuki W, Nakamura T, Tsushima H (2016) Improving the constraint on the Mw7.1 off-Fukushima shallow normal-faulting earthquake with the high azimuthal coverage tsunami data from the S-net wide and dense network: implication for the stress regime in the Tohoku overriding plate. J Geophys Res Solid Earth 126:e2021JB022223. https://doi.org/10.1029/2021JB022223
Kubota T, Saito T, Suzuki W (2020) Millimeter-scale tsunami detected by a wide and dense observation array in the deep ocean: fault modeling of an Mw 6.0 interplate earthquake off Sanriku NE Japan. Geophys Res Lett 47:e2019GL085842. https://doi.org/10.1029/2019GL085842
Liu CM, Rim D, Baraldi R, LeVeque RJ (2021) Comparison of machine learning approaches for tsunami forecasting from sparse observations. Pure Appl Geophys 178:5129–5153. https://doi.org/10.1007/s00024-021-02615-2
Maeda T, Obara K, Shinohara M, Kanazawa T, Uehira K (2015) Successive estimation of a tsunami wavefield without earthquake source data: a data assimilation approach toward real-time tsunami forecasting. Geophys Res Lett 42:7923–7932. https://doi.org/10.1002/2015GL065588
Maeda T (2016) Instantaneous separation between coseismic deformation and tsunami height from pressure gauge records based on the data assimilation method. In 2016 American Geophysical Union Fall Meeting, San Francisco, USA,
Mai PM, Thingbaijam KKS (2014) SRCMOD: an online database of finite fault rupture models. Seismol Res Lett 85:1348–1357. https://doi.org/10.1785/0220140077
Makinoshima F, Oishi Y, Yamazaki T, Furumura T, Imamura F (2021) Early forecasting of tsunami inundation from tsunami and geodetic observation data with convolutional neural networks. Nat Commun 12:2253. https://doi.org/10.1038/s41467-021-22348-0
Mofjeld HO (1997) Tsunami detection algorithm, not published paper. http://nctr.pmel.noaa.gov/tda_documentation.html. Accessed 12 December 2022.
Mulia IE, Gusman AR, Satake K (2020) Applying a deep learning algorithm to tsunami inundation database of megathrust earthquakes. J Geophys Res Solid Earth 125:e2020JB019690. https://doi.org/10.1029/2020JB019690
Mulia IE, Ueda N, Miyoshi T, Gusman AR, Satake K (2022) Machine learning-based tsunami inundation prediction derived from offshore observations. Nat Commun 13:5489. https://doi.org/10.1038/s41467-022-33253-5
Okada Y (1992) Internal deformation due to shear and tensile faults in a half-space. Bull Seismol Soc Am 82:1018–1040. https://doi.org/10.1785/BSSA0820021018
Rim D, Baraldi R, Liu CM, LeVeque RJ, Terada K (2022) Tsunami early warning from global navigation satellite system data using convolutional neural networks. Geophys Res Lett 49:e2022GL099511. https://doi.org/10.1029/2022GL099511
Tanioka Y, Yamanaka Y, Nakagaki T (2022) Characteristics of the deep sea tsunami excited offshore Japan due to the air wave from the 2022 Tonga eruption. Earth Planets Space 74:61. https://doi.org/10.1186/s40623-022-01614-5
Tsushima H, Hino R, Fujimoto H, Tanioka Y, Imamura F (2009) Near-field tsunami forecasting from cabled ocean bottom pressure data. J Geophys Res Solid Earth 114:B06309. https://doi.org/10.1029/2008JB005988
Tsushima H, Hino R, Tanioka Y, Imamura F, Fujimoto H (2012) Tsunami waveform inversion incorporating permanent seafloor deformation and its application to tsunami forecasting. J Geophys Res Solid Earth 117:B03311. https://doi.org/10.1029/2011JB008877
Wang Y, Satake K (2021) Real-time tsunami data assimilation of s-net pressure gauge records during the 2016 Fukushima earthquake. Seismol Res Lett 92:2145–2155. https://doi.org/10.1785/0220200447
Wang Y, Satake K, Maeda T, Shinohara M, Sakai S (2020) A method of real-time tsunami detection using ensemble empirical mode decomposition. Seismol Res Lett 91:2851–2861. https://doi.org/10.1785/0220200115
Wang Y, Imai K, Mulia IE, Ariyoshi K, Takahashi N, Sasaki K, Kaneko H, Abe H, Sato Y (2023) Data assimilation using high-frequency radar for tsunami early warning: a case study of the 2022 Tonga volcanic tsunami. J Geophys Res Solid Earth 128:e2022JB025153. https://doi.org/10.1029/2022JB025153
Yoshimoto M, Watada S, Fujii Y, Satake K (2016) Source estimate and tsunami forecast from far-field deep-ocean tsunami waveforms—the 27 february 2010 Mw 8.8 Maule earthquake. Geophys Res Lett 43:659–665. https://doi.org/10.1002/2015GL067181
Zhou C, Paffenroth RC (2017) Anomaly detection with robust deep autoencoders. In: KDD'17: proceedings of the 23rd ACM SIGKDD international conference on knowledge discovery and data mining, Halifax, Nova Scotia, Canada. pp. 665–674. https://doi.org/10.1145/3097983.3098052.

Publisher's Note